

Machine Learning of Topological Insulator and Anderson Insulator in One-Dimensional Extended Su-Schrieffer-Heeger Chain

Zhekai Yin

Department of Physics, Xiamen University Malaysia, 43900 Sepang, Selangor, Malaysia

C. K. Ong*

*Department of Physics, Xiamen University Malaysia, 43900 Sepang, Selangor, Malaysia and
Key Laboratory for Magnetism and Magnetic Materials of the
Ministry of Education, Lanzhou University, Lanzhou 730000, China*

(Dated: March 13, 2026)

We study disorder effects in the extended Su–Schrieffer–Heeger (SSH) model using a convolutional neural network (CNN) trained on reduced correlation matrices (RCMs) of disorder-free systems to predict winding number phase diagrams in systems with off-diagonal and diagonal disorder. The trained CNN model generalizes to chiral-symmetry-preserving off-diagonal disorder system but fails in the presence of chiral-symmetry-breaking diagonal disorder system. Using principal component analysis (PCA) of the RCM feature space, we demonstrate that disorder-free and symmetry-preserving systems share overlapping feature manifolds, whereas symmetry-breaking disorder causes them to diverge. Inverse participation ratio (IPR) and energy spectrum analysis further demonstrate that off-diagonal disorder preserves topological edge states, whereas diagonal disorder drives a transition to an Anderson insulator. Our results position machine learning not merely as a classifier, but as a sensitive probe for the symmetry-protected nature of quantum matter.

I. INTRODUCTION

Topological insulators, characterized by topological invariants and robust boundary states[1, 2], and Anderson insulators, characterized by bulk state localization[3, 4], have reshaped our understanding of quantum materials[5]. The Su–Schrieffer–Heeger (SSH) model provides a paradigmatic one-dimensional example, where localized edge states are protected by chiral symmetry and classified by an integer winding number[6–8]. The SSH can be extended to include diagonal disorder and off-diagonal disorder to examine effects of various perturbations. In the diagonal disorder perturbation, the chiral symmetry of the linear chain remains intact and exhibits topological phase transition. In the off-diagonal disorder perturbation, the chiral symmetry of the linear chain is broken and bulk localizations appear, exhibiting Anderson insulator transition.

In this paper, we train a supervised convolutional neural network (CNN) on analytic reduced correlation matrices (RCMs) of disorder-free SSH models with long-range hopping as input data set, together with three winding numbers ($\nu \in \{0, 1, 2\}$) as targets. The trained CNN model is then generalized to study out-of-distribution (OOD) systems, successfully predicting the phase diagram for off-diagonal disorder system while failing to do so for diagonal disorder system. These results are consistent with the literature reported previously[9, 10]. In order to understand the role of chiral symmetry playing in space feature extraction in CNN technique, we perform principal component analysis (PCA) of the RCM feature

space, which reveals overlapping manifolds for disorder-free and symmetry-preserving disorder systems, but exhibits a clear separation when symmetry is broken.

To investigate why the CNN fails to generalize to OOD cases where symmetry is broken, we note that PCA merely classifies the similarity of feature distributions rather than their physical nature. We, therefore, proceed to study the localization properties of single-particle eigenstates via inverse participation (IPR) and the energy spectrum across the hopping parameters. It shows that edge states survive only in the presence of chiral symmetry, while diagonal disorder breaks the chiral symmetry and drives a transition to an Anderson insulator.

II. SU-SCHRIEFFER-HEEGER MODEL

A. Hamiltonian

We consider an extended Su–Schrieffer–Heeger (SSH) model on a one-dimensional chain with N unit cells (total $2N$ sites) under open boundary conditions (OBC). The Hamiltonian in real space is:

$$\hat{H} = \sum_{n=1}^N \left(t_{1,n} \hat{c}_{n,A}^\dagger \hat{c}_{n,B} + \text{h.c.} \right) + \sum_{n=1}^{N-1} \left(t_{2,n} \hat{c}_{n,B}^\dagger \hat{c}_{n+1,A} + \text{h.c.} \right) + t_3 \sum_{n=1}^{N-2} \left(\hat{c}_{n,A}^\dagger \hat{c}_{n+2,B} + \text{h.c.} \right) + \sum_{i=1}^{2N} V_i \hat{c}_i^\dagger \hat{c}_i, \quad (1)$$

where $\hat{c}_{n,\alpha}$ ($\alpha = A, B$) creates a spinless fermion on sublattice α of the n -th unit cell. The first two terms describe the standard dimerized hopping, where $t_{1,n}$ is the intra-cell amplitude and $t_{2,n}$ is the inter-cell amplitude.

* ckong@xmu.edu.my

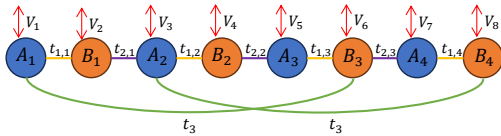


FIG. 1: Schematic diagram of SSH model with long range hopping. A_i, B_i are sites of the i -th unit cell. $\{t_{1,1}, t_{1,2}, t_{1,3}, \dots\}$ are the intra-cell hopping amplitudes, $\{t_{2,1}, t_{2,2}, t_{2,3}, \dots\}$ are the inter-cell hopping amplitudes, t_3 is the long range hopping amplitude, $\{V_1, V_2, V_3, \dots\}$ are the on-site potentials.

We introduce a long range hopping t_3 between A_n and B_{n+2} , which extends the model beyond the conventional binary topological classification. V_i describes the on-site potential at each site i , which accounts for external electric fields or structural inhomogeneities in the 1D chain. Disorder is incorporated via random modulations:

$$t_{1,n} = t_1 + W_1\omega_n^{(1)}, \quad t_{2,n} = t_2 + W_2\omega_n^{(2)}, \quad V_i = V_{\text{on}}\omega_i^{(3)}, \quad (2)$$

where the variables ω are independent and identically distributed (i.i.d.) according to a uniform distribution on the interval $[-0.5, 0.5]$. The parameters W_1, W_2 control off-diagonal disorder strength, while V_{on} introduces diagonal (on-site) disorder strength. The structure of this long range hopping SSH model is sketched in Fig. 1.

B. Winding Number

In the disorder-free model ($W_1 = W_2 = V_{\text{on}} = 0$), the system is translationally invariant. Under periodic boundary conditions (PBC), the Bloch Hamiltonian is:

$$H(k) = \begin{pmatrix} 0 & h^*(k) \\ h(k) & 0 \end{pmatrix}, \quad h(k) = t_1 + t_2 e^{-ik} + t_3 e^{-i2k}. \quad (3)$$

The system belongs to the chiral (AIII) symmetry class [11, 12] and is characterized by the integer winding number:

$$\nu = \frac{1}{2\pi i} \oint_{\text{BZ}} dk \partial_k \ln h(k), \quad (4)$$

which counts the number of times the complex function $h(k)$ winds around the origin as k traverses the Brillouin zone. According to Cauchy Argument Principle[13–15], the winding of a complex function around the origin is related to its zeros and poles inside a closed contour. Specifically, the integrand $\partial_k \ln h(k)$ in Eq. (4) maps the unit circle in the z -plane ($z = e^{ik}$) to the winding of the characteristic polynomial $t_3 z^2 + t_2 z + t_1$ in the complex h -plane. Hence, the winding number ν is fully determined by the number of roots of the polynomial $t_3 z^2 + t_2 z + t_1 = 0$ that lie inside the unit circle ($|z| < 1$). This yields a

rich phase diagram with three distinct topological sectors ($\nu \in \{0, 1, 2\}$), in contrast to the standard SSH model ($t_3 = 0$) which only supports $\nu = 0$ or 1.

In the disorder-free model, the winding number ν is rigorously defined under PBC via the momentum-space Bloch Hamiltonian (Eq. (4)). However, experimental probes and numerical simulations of real materials are typically performed under OBC, where the system exhibits edge states and lacks translational symmetry. Therefore, it doesn't have a well-defined Brillouin zone. However, following the bulk–boundary correspondence, the number of zero-energy edge states under OBC is strictly determined by the bulk winding number ν calculated under PBC[16]. In our machine learning training, we therefore use PBC-computed ν as label together with OBC-derived reduced correlation matrix (RCM) as the input data set.

C. Symmetry and Stability Under Disorder

The topological classification in Eq. (4) relies crucially on chiral symmetry, which requires the Hamiltonian to be off-diagonal in a suitable basis. This symmetry is preserved when only off-diagonal disorder is present ($V_{\text{on}} = 0$). In this case, the winding number remains well-defined, and the system exhibits a symmetry-protected topological phase robust against weak disorder [17–19]. By contrast, diagonal disorder ($V_{\text{on}} \neq 0$) explicitly breaks chiral symmetry. Consequently, the bulk–boundary correspondence breaks down, and the topological phase diagram collapses into a featureless insulating regime dominated by Anderson localization [3, 20–22]. This difference between robustness under symmetry-preserving disorder and fragility under symmetry-breaking disorder will serve as the central physical principle to interpret the out-of-distribution (OOD) generalization behavior of our machine learning model in Sec. IV. Specifically, OOD generalization[23, 24] refers to the CNN's ability to correctly identify topological phases when tested on disordered configurations that are entirely absent from the disorder-free training set.

III. CONVOLUTIONAL NEURAL NETWORK (CNN)

We employ a supervised 2D CNN to classify the topological phases of the system. The model uses RCMs as the input data, mapping it to winding number $\nu \in \{0, 1, 2\}$. The primary aim is to evaluate the model's OOD generalization.

A. Input Data: Reduced Correlation Matrix (RCM)

We employ the single-particle correlation matrix (RCM) as the input data for our CNN. For a non-interacting system at half-filling, the many-body ground state $|\Psi_0\rangle$ is a Slater determinant fully characterized by the correlation matrix $C_{ij} = \langle \Psi_0 | \hat{c}_i^\dagger \hat{c}_j | \Psi_0 \rangle$. In practice, C is constructed as a projection operator onto the subspace of the N occupied single-particle eigenstates:

$$C = \sum_{n=1}^N |\psi_n\rangle \langle \psi_n|, \quad (5)$$

where $\{|\psi_n\rangle\}$ are the N lowest-energy eigenstates obtained from the diagonalization of the single-particle Hamiltonian. To reduce the input dimensionality while preserving topological signatures, we define our input data $C_{\text{sub}} \in \mathbb{R}^{N \times N}$ as the sub-block of C restricted to sublattice A .

As the input for our CNN, we utilize the RCM C_{sub} , which serves as a computationally efficient representation of the many-body reduced density matrix (RDM). Because our system consists of non-interacting fermions, C_{sub} contains the complete information of the RDM via the single-particle entanglement spectrum. Thus, by training on C_{sub} , the network is effectively learning the entanglement spectrum $\{\xi_k\}$ that characterize the topological phases[25–28].

B. CNN Architecture

Our classifier is a standard 2D CNN[29–31], illustrated in Fig. 2. The input to the network is the $N \times N$ RCM ($N = 40$), treated as a single-channel grayscale image and reshaped into a tensor of size $1 \times N \times N$. The architecture comprises three convolutional blocks: each block contains a 3×3 convolutional layer with zero padding, followed by a ReLU activation; max-pooling with kernel size 2×2 is applied after the second and third blocks, progressively reducing the spatial dimensions from $40 \rightarrow 20 \rightarrow 10$. The resulting feature maps (of size $64 \times 10 \times 10$) are flattened into a 6400-dimensional vector and passed through two fully connected layers ($6400 \rightarrow 256 \rightarrow 3$) with ReLU activation after the first fully connected layer. The final layer outputs three numerical numbers for the three winding number classes $\nu = 0, 1, 2$. These are the raw numbers the model calculates for each winding number before they are converted into actual probabilities using softmax function.

The model is trained exclusively on the disorder-free system data set using the Adam optimizer and cross-entropy loss:

$$\mathcal{L} = -\frac{1}{|\mathcal{S}|} \sum_{(x,y) \in \mathcal{S}} \sum_{k=0}^2 \mathbb{I}(y = k) \log p_k(x), \quad (6)$$

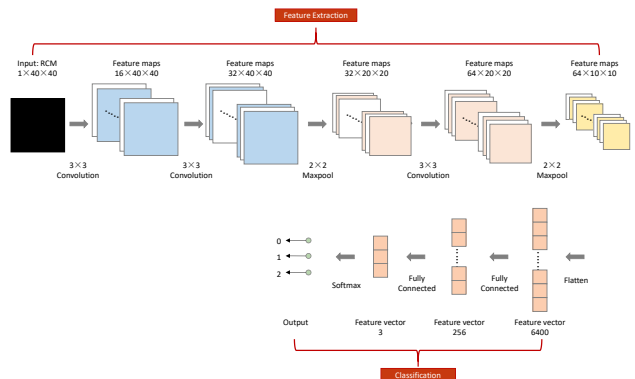


FIG. 2: Schematic diagram of CNN architecture. The input is RCM of size $1 \times 40 \times 40$. The feature extraction stage consists of three convolutional layers (using 3×3 kernels) and two max-pooling layers (using 2×2 kernels) to progressively extract high-level topological features while reducing spatial dimensionality. The final feature maps of size $64 \times 10 \times 10$ are flattened into a 6400-dimensional feature vector. This vector is passed through two fully connected layers, reducing the dimensionality to 256 and finally to 3. A Softmax activation function is applied at the output layer to provide the predicted probabilities for winding numbers $\{0, 1, 2\}$.

where \mathcal{S} denotes the input dataset, x is the RCMs, $y \in \{0, 1, 2\}$ is the true winding number label, $p_k(x)$ is the predicted probability for class k (obtained via softmax), and $\mathbb{I}(\cdot)$ is the indicator function. Specifically, $\mathbb{I}(y = k)$ yields 1 if the true winding number y matches the class index k , and 0 otherwise. Training employs early stopping when the loss falls below 10^{-5} .

IV. CNN PREDICTIONS UNDER DISORDER

The training data set is constructed from the disorder-free SSH model, where the Hamiltonian parameters are uniformly sampled within the range $t_1, t_2 \in [-2, 2]$. For each parameter point (t_1, t_2) , we compute the RCM as described in Sec. III A. And each RCM is labeled with its corresponding winding number ν , calculated by the method in Sec. II B.

The winding number phase diagram for this disorder-free SSH model is presented in Fig. 3.

To evaluate the generalization ability of the trained CNN, we subject the model to both off-diagonal and diagonal disorder regimes. For each disordered configuration, we compute the corresponding RCM and feed it as input into the network. The CNN then maps it to winding number. By scanning the (t_1, t_2) parameter space under varying disorder strengths, we construct predicted phase diagrams of the winding number ν .

Crucially, for each disordered configuration, we perform an ensemble average over $K = 50$ disorder re-

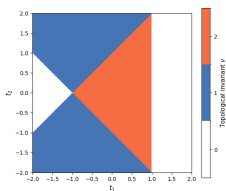


FIG. 3: Analytical winding number map of disorder-free system

alizations, computing the mean softmax probability $\bar{p}(\nu)$. From this, we extract (i) the predicted class $\nu_{\text{pred}} = \arg \max_{\nu} \bar{p}(\nu)$, (ii) the confidence $\max_{\nu} \bar{p}(\nu)$, and (iii) the normalized entropy $\frac{H(\bar{p})}{\log 3}$ with $H(\bar{p}) = -\sum_{\nu} \bar{p}(\nu) \log \bar{p}(\nu)$.

The ensemble-averaged confidence quantifies the robustness of topological signatures in the RCM against disorder: high values (> 0.9) indicate that edge-state correlations remain dominant across disorder realizations, while low confidence signals proximity to phase boundaries or symmetry-breaking regimes where topological features become ambiguous. Conversely, the normalized entropy measures topological mixing induced by disorder—peaking when individual realizations fluctuate between distinct winding numbers (e.g., residual edge modes competing with bulk localization), thereby serving as an indicator of symmetry-breaking transitions where chiral protection fails.

A. OOD Prediction for Off-Diagonal Disorder Case

We first apply off-diagonal disorder, which preserves chiral symmetry. We set different values for off-diagonal disorder strength ($W_{\text{off}} = W_1 = W_2 = 0.1, 1.0, 2.0, 3.0, 4.0, 5.0$), while $V_{\text{on}} = 0$. Under this condition, the winding number remains a well-defined topological invariant, and the phase diagram is expected to persist, with critical regions broadened by disorder-induced fluctuations.

As shown in Fig. 4a for $W_{\text{off}} = 0.1$, the CNN’s predicted phase map remains strikingly similar to the disorder-free case. All three topological sectors are clearly identifiable, and phase boundaries align closely with the analytical disorder-free critical lines. The confidence (Fig. 4b) is high deep within each phase and drops only near boundaries, while the entropy (Fig. 4c) peaks precisely in those transition regions. This behavior originates from the closing of the topological gap at criticality: at phase boundaries the bulk gap vanishes, causing edge states to hybridize with the continuum and rendering RCM features ambiguous between competing winding numbers. Deep within a phase, by contrast, the finite topological gap protects edge-state signatures in the RCM, ensuring consistent classification across disorder realizations.

As W_{off} increases (see Appendix A), the boundaries grad-

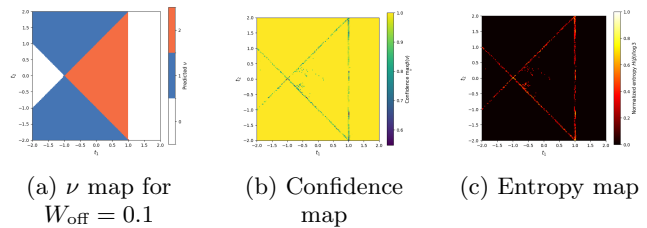


FIG. 4: Visualization results for $W_{\text{off}} = 0.1$: (a) winding number ν map, boundary is the same as disorder-free system, (b) confidence map indicating prediction certainty, confidence is very high throughout the map, (c) entropy map representing prediction uncertainty, entropy is very low throughout the map.

ually blur, but the topological structure remains accurate until $W_{\text{off}} \approx 3.0$.

This demonstrates that the CNN naturally generalizes to symmetry-preserving disorder. It does not merely memorize disorder-free features; it has learned a representation that is physically robust because the underlying topological classification itself is robust.

B. OOD Prediction for Diagonal Disorder Case

Next, we introduce diagonal disorder $V_{\text{on}} = 0.1$, while $W_{\text{off}} = 0$. This breaks chiral symmetry, the predicted topological structure collapses completely, even though the introduced diagonal disorder is tiny. As shown in Fig. 5a for $V_{\text{on}} = 0.1$, the phase map becomes spatially chaotic, with no discernible topological sectors. The confidence is uniformly low (Fig. 5b), and the entropy is high across the entire parameter space (Fig. 5c), indicating maximal uncertainty. This failure is not a flaw

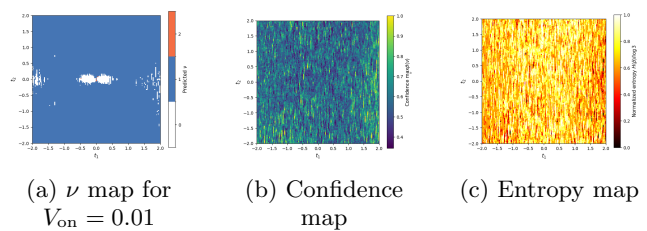


FIG. 5: Visualization results for $V_{\text{on}} = 0.1$: (a) winding number ν map, no phase boundary can be observed, (b) confidence map indicating prediction certainty, confidence is very low throughout the map, (c) entropy map representing prediction uncertainty, entropy is very high throughout the map.

of the CNN—it is physically correct. In the absence of chiral symmetry, the winding number ν is no longer a conserved quantity[18, 19, 32]; the bulk-boundary correspondence breaks down, and the system transitions into an Anderson insulator, which will be discussed in Sec. VI.

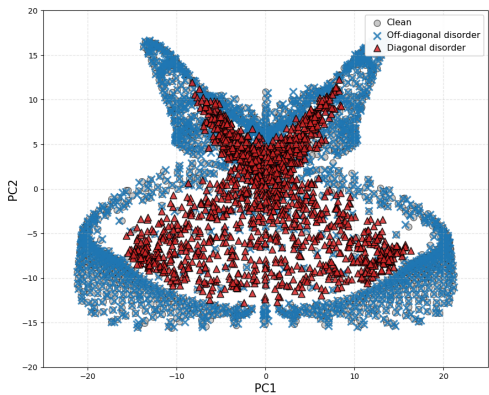


FIG. 6: PCA visualizations of RCM spaces. The feature distribution of disorder-free (gray circles) and off-diagonal disorder (blue crosses) samples exhibit substantial overlap in PCA space, while diagonal disorder samples (red circles) diverge.

There is no true topological phase structure to predict. The CNN’s high entropy and low confidence thus serve as a sensitive diagnostic of symmetry breaking and the consequent loss of topological order.

V. PCA ANALYSIS OF RCM FEATURE SPACE

To elucidate the physical origin of the CNN’s OOD generalization, we analyze the geometry of the RCM feature space under distinct disorder types using PCA[33–35]. RCMs from three ensembles—disorder-free system ($W_{\text{off}} = V_{\text{on}} = 0$), off-diagonal disorder system ($W_{\text{off}} = 0.1, V_{\text{on}} = 0$), and diagonal disorder system ($W_{\text{off}} = 0, V_{\text{on}} = 0.1$)—are standardized and projected onto the first two principal components, which collectively explain 71.3% of the total variance (Fig. 6).

The feature distributions of disorder-free and off-diagonal disorder samples exhibit substantial overlap in PCA space, demonstrating that the RCM manifold is topologically invariant under symmetry-preserving perturbations. Despite fluctuations in hopping amplitudes, the topological signatures encoded in the RCM remain robust because the chiral symmetry is preserved. Consequently, the CNN trained on data of disorder-free system can generalize to off-diagonal disordered model.

In contrast, diagonal disorder triggers a transition from topological insulator to Anderson insulator, manifested as a clear geometric separation between disorder-free and disordered samples in feature space, even at $V_{\text{on}} = 0.1$. This geometric shift explains why the CNN’s OOD generalization is not applicable in diagonal disordered model.

VI. EDGE STATES, LOCALIZATION, AND SYMMETRY BREAKING

In order to shed some light on chiral symmetry preservation manifesting feature overlap while chiral symmetry breaking induces feature space separation, we probe the localization properties of single-particle eigenstates using two complementary diagnostics—IPR and the energy spectrum—across the (t_1, t_2) parameter space. These quantities directly distinguish topological insulator from Anderson insulator.

A. IPR as Spectral Diagnostics

For a normalized eigenstate $|\phi_n\rangle = \sum_i \psi_n(i)|i\rangle$ of the Hamiltonian H , IPR is defined as:

$$\text{IPR}(\phi_n) = \sum_{i=1}^{2N} |\psi_n(i)|^4 \quad (7)$$

where $N = 40$ is the number of unit cells.

The IPR serves as a robust numerical probe for spatial localization, allowing one to identify localized edge modes and distinguish them from extended bulk states[36, 37]. In disordered systems, large IPR values further signal Anderson localization.[38–42].

We compute the full energy spectrum $\{E_n\}$ and the corresponding IPR values $\{\text{IPR}(\phi_n)\}$ for each disorder realization. All results are averaged over 50 independent realizations to suppress sample-to-sample fluctuations while preserving universal signatures.

B. Energy Spectrum of Disorder-free, Off-diagonal Disorder and Diagonal Disorder Cases

Fig. 7 shows the energy spectrum colored by IPR across the t_1 parameter space ($-2 < t_1 < 2$) at fixed $t_2 = 0, t_3 = 1.0$, comparing three cases: disorder-free (a), off-diagonal disorder $W_{\text{off}} = 0.1$ (b), and diagonal disorder $V_{\text{on}} = 0.1$ (c). From Fig. 3, we know that in the disorder-free case, the system exhibits a topological phase with winding number $\nu \neq 0$ for $|t_1| < 1$, while for $|t_1| > 1$, the system transitions to a trivial state ($\nu = 0$).

In the disorder-free case (Fig. 7a), degenerate zero-energy modes ($E = 0$) emerge precisely within the topological region ($-1.0 < t_1 < 1.0$). These modes exhibit IPR values significantly higher than the bulk states, characteristic of well-defined edge states. Under off-diagonal disorder (Fig. 7b), these zero-energy modes persist robustly across the topological phase. Their energy remains pinned at the Fermi level ($E = 0$) and their IPR remains high, confirming that the system remains a topological insulator with its chiral-symmetry-protected topology surviving despite disorder-induced bulk spectral fluctuations [36, 39].

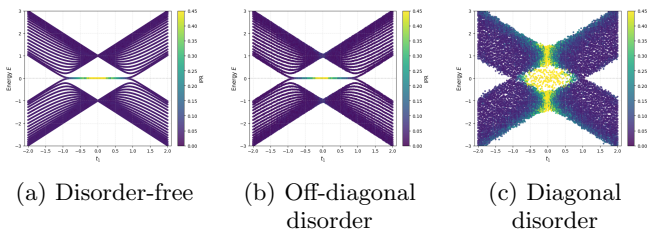


FIG. 7: Energy spectrum with IPR coloring for SSH model with long-range hopping $t_3 = 1.0$. (a) Disorder-free system, edge states exist, bulk localizations don't exist. (b) Off-diagonal disorder with $W_{\text{off}} = 0.1$, edge states exist, bulk localizations don't exist. (c) Diagonal disorder with $V_{\text{on}} = 0.1$, edge states disappear, bulk localizations appear. The color indicates IPR values.

In contrast, diagonal disorder (Fig. 7c) destroys the topological signatures even at weak strengths. The previously degenerate edge modes are shifted from zero energy and hybridize with the bulk. Notably, the IPR increases compared with disorder-free system and off-diagonal disordered system, signaling a transition where the system's localization mechanism shifts from topological edge protection to Anderson localization across the entire spectrum. This spectral collapse and the loss of mid-gap states provide the structural origin for the PCA manifold separation discussed in Sec. V: once chiral symmetry is broken, the RCM loses the distinct boundary-bulk correlations that define the topological manifold. Consequently, the CNN's OOD generalizations is not applicable in diagonal disordered model with chiral symmetry broken because this system has undergone a phase transition into an Anderson insulator.

C. Energy Spectrum of Different Off-diagonal and Diagonal Disorder Strengths

To quantify the robustness of edge states, Fig. 8 tracks spectral evolution at a fixed topological point ($t_1 = 0.1, t_2 = 0, t_3 = 1.0$) as disorder strength increases. Under off-diagonal disorder (Fig. 8a), the zero-energy modes remain pinned at $E = 0$ even if the disorder strength becomes larger, with bulk states' IPR staying low throughout. This confirms that the system remains a topological insulator with its edge-state signatures intact.

Under diagonal disorder (Fig. 8b), however, even infinitesimal V_{on} triggers immediate shift of the zero-energy modes. As V_{on} increases, the entire spectrum undergoes a disorder-driven localization transition. By $V_{\text{on}} \approx 2.0$, all states exhibit high IPR values, signaling that the system has fully evolved from a topological phase into an

Anderson insulating phase [5, 43, 44]. This topological collapse at arbitrarily weak symmetry breaking disorder provides the structural explanation for the CNN's catastrophic failure discussed in Sec. IV. Because the RCM's structure is fundamentally tethered to these symmetry-protected edge states, their immediate dissolution under diagonal disorder means the CNN is presented with data that no longer contains the "topological fingerprints" it was trained to recognize. Therefore, the CNN's failure is not a limitation of the model architecture, but a direct reflection of the fundamental breakdown of symmetry-protected features at the microscopic level.

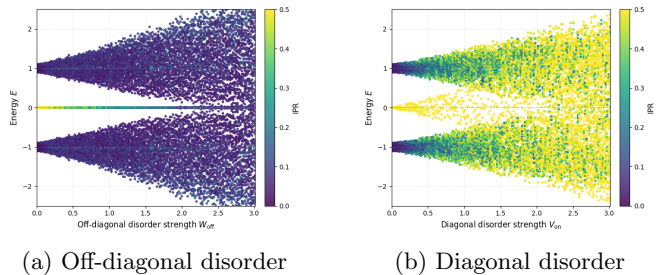


FIG. 8: Effect of disorder on energy spectrum and IPR ($t_1 = 0.1, t_2 = 0.0, t_3 = 1.0$). (a) Off-diagonal disorder (W_{off}). Edge states exist persistently, bulk states are not localized. (b) Diagonal disorder (V_{on}). Edge states disappear, bulk states become localized. The color indicates IPR values.

VII. CONCLUSION

In summary, our work establishes that the OOD generalization of machine learning in topological systems is fundamentally governed by the underlying physical symmetry. We show that the machine learning achieves seamless OOD success as long as chiral symmetry is preserved, maintaining the system as a topological insulator; conversely, it fails when chiral symmetry is broken, as the system transitions into an Anderson insulator.

PCA shows that symmetry preservation ensures an overlap of feature manifolds, while symmetry breaking induces the separation. Finally, IPR and energy spectrum analysis provides the structural evidence, confirming that the "learning failure" is a direct reflection of the dissolution of topological edge states into localized bulk states. Ultimately, our results position machine learning not merely as a classifier, but as a sensitive probe for the symmetry-protected nature of quantum matter.

Appendix A: Supplementary Plots for Other W_{off} Values

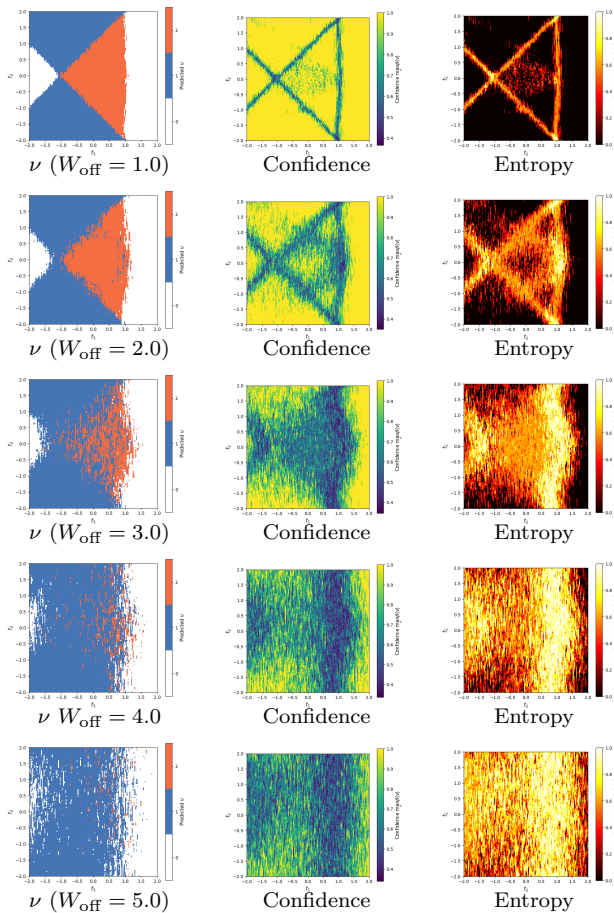


FIG. 9: Prediction results for varying disorder strengths (W_{off}). From top to bottom: row 1: $W_{\text{off}} = 1.0$, row 2: $W_{\text{off}} = 2.0$, row 3: $W_{\text{off}} = 3.0$, row 4: $W_{\text{off}} = 4.0$, row 5: $W_{\text{off}} = 5.0$. From left to right: (1) predicted winding number maps, as W_{off} increases, boundaries gradually blur, but the topological structure remains accurate until $W_{\text{off}} \approx 3.0$, (2) confidence maps indicating prediction certainty, as W_{off} increase, confidence decreases, (3) entropy maps representing prediction uncertainty, as W_{off} increases, entropy increases.

-
- [1] M. Z. Hasan and C. L. Kane, Colloquium: topological insulators, *Reviews of modern physics* **82**, 3045 (2010).
- [2] X.-L. Qi and S.-C. Zhang, Topological insulators and superconductors, *Reviews of modern physics* **83**, 1057 (2011).
- [3] P. W. Anderson *et al.*, Absence of diffusion in certain random lattices, *Physical review* **109**, 1492 (1958).
- [4] E. Abrahams, P. W. Anderson, D. C. Licciardello, and T. V. Ramakrishnan, Scaling theory of localization: Absence of quantum diffusion in two dimensions, *Physical Review Letters* **42**, 673 (1979).
- [5] J. Li, R.-L. Chu, J. K. Jain, and S.-Q. Shen, Topological anderson insulator, *Physical review letters* **102**, 136806 (2009).
- [6] L. Li, Z. Xu, and S. Chen, Topological phases of generalized su-schrieffer-heeger models, *Physical Review B* **89**, 085111 (2014).
- [7] E. J. Meier, F. A. An, and B. Gadway, Observation of the topological soliton state in the su-schrieffer-heeger model, *Nature communications* **7**, 13986 (2016).
- [8] J. K. Asbóth, L. Oroszlány, and A. Pályi, The su-schrieffer-heeger (ssh) model, in *A short course on topological insulators: band structure and edge states in one and two dimensions* (Springer, 2016) pp. 1–22.
- [9] W. A. Benalcazar and A. Cerjan, Chiral-symmetric higher-order topological phases of matter, *Physical Review Letters* **128**, 127601 (2022).
- [10] E. J. Meier, F. A. An, A. Dauphin, M. Maffei, P. Massig-

- nan, T. L. Hughes, and B. Gadway, Observation of the topological anderson insulator in disordered atomic wires, *Science* **362**, 929 (2018).
- [11] J. Shapiro and M. I. Weinstein, Is the continuum ssh model topological?, *Journal of Mathematical Physics* **63** (2022).
- [12] S.-H. Han, S.-G. Jeong, S.-W. Kim, T.-H. Kim, and S. Cheon, Topological features of ground states and topological solitons in generalized su-schrieffer-heeger models using generalized time-reversal, particle-hole, and chiral symmetries, *Physical Review B* **102**, 235411 (2020).
- [13] L. V. Ahlfors and L. V. Ahlfors, *Complex analysis*, Vol. 3 (McGraw-Hill New York, 1979).
- [14] B.-H. Chen and D.-W. Chiou, An elementary rigorous proof of bulk-boundary correspondence in the generalized su-schrieffer-heeger model, *Physics Letters A* **384**, 126168 (2020).
- [15] C.-S. Lee, I.-F. Io, and H.-c. Kao, Winding number and zak phase in multi-band ssh models, *Chinese Journal of Physics* **78**, 96 (2022).
- [16] J. K. Asbóth, L. Oroszlány, and A. Pályi, *A short course on topological insulators*, Vol. 919 (Springer, 2016).
- [17] J. Cayssol, B. Dóra, F. Simon, and R. Moessner, Floquet topological insulators, *physica status solidi (RRL)—Rapid Research Letters* **7**, 101 (2013).
- [18] E. Prodan, Disordered topological insulators: a non-commutative geometry perspective, *Journal of Physics A: Mathematical and Theoretical* **44**, 113001 (2011).
- [19] B. A. Bernevig, *Topological insulators and topological superconductors* (Princeton university press, 2013).
- [20] Y. Hatsugai, Edge states in the integer quantum hall effect and the riemann surface of the bloch function, *Physical Review B* **48**, 11851 (1993).
- [21] C. Max, *Bulk-boundary correspondence of disordered topological insulators and superconductors*, Ph.D. thesis, Universität zu Köln (2019).
- [22] P. A. Lee and T. V. Ramakrishnan, Disordered electronic systems, *Reviews of modern physics* **57**, 287 (1985).
- [23] K. Cybiński, M. Płodzień, M. Tomza, M. Lewenstein, A. Dauphin, and A. Dawid, Characterizing out-of-distribution generalization of neural networks: application to the disordered su-schrieffer-heeger model, *Machine Learning: Science and Technology* **6**, 015014 (2025).
- [24] P. Zhang, H. Shen, and H. Zhai, Machine learning topological invariants with neural networks, *Physical review letters* **120**, 066401 (2018).
- [25] I. Peschel, Calculation of reduced density matrices from correlation functions, *Journal of Physics A: Mathematical and General* **36**, L205 (2003).
- [26] I. Peschel and V. Eisler, Reduced density matrices and entanglement entropy in free lattice models, *Journal of physics a: mathematical and theoretical* **42**, 504003 (2009).
- [27] M.-C. Chung and I. Peschel, Density-matrix spectra for two-dimensional quantum systems, *Physical Review B* **62**, 4191 (2000).
- [28] N. Crampé, K. Guo, and L. Vinet, Entanglement of free fermions on hadamard graphs, *Nuclear Physics B* **960**, 115176 (2020).
- [29] K. O’shea and R. Nash, An introduction to convolutional neural networks, arXiv preprint arXiv:1511.08458 (2015).
- [30] J. Wu, Introduction to convolutional neural networks, National Key Lab for Novel Software Technology. Nanjing University. China **5**, 495 (2017).
- [31] J. Bouvrie, Notes on convolutional neural networks, (2006).
- [32] A. Kitaev, Periodic table for topological insulators and superconductors, in *AIP conference proceedings*, Vol. 1134 (American Institute of Physics, 2009) pp. 22–30.
- [33] H. Abdi and L. J. Williams, Principal component analysis, *Wiley interdisciplinary reviews: computational statistics* **2**, 433 (2010).
- [34] S. Wold, K. Esbensen, and P. Geladi, Principal component analysis, *Chemometrics and intelligent laboratory systems* **2**, 37 (1987).
- [35] R. Bro and A. K. Smilde, Principal component analysis, *Analytical methods* **6**, 2812 (2014).
- [36] N. Murphy, R. Wortis, and W. Atkinson, Generalized inverse participation ratio as a possible measure of localization for interacting systems, *Physical Review B—Condensed Matter and Materials Physics* **83**, 184206 (2011).
- [37] S. Ghosh and S. Roy, Exploring topological and localization phenomena in ssh chains under generalized aah modulation: A computational approach, arXiv preprint arXiv:2506.10195 (2025).
- [38] M. Calixto and E. Romera, Inverse participation ratio and localization in topological insulator phase transitions, *Journal of Statistical Mechanics: Theory and Experiment* **2015**, P06029 (2015).
- [39] F. Evers and A. Mirlin, Fluctuations of the inverse participation ratio at the anderson transition, *Physical review letters* **84**, 3690 (2000).
- [40] P. Shukla, Disorder perturbed flat bands: Level density and inverse participation ratio, *Physical Review B* **98**, 054206 (2018).
- [41] J. Bauer, T.-M. Chang, and J. Skinner, Correlation length and inverse-participation-ratio exponents and multifractal structure for anderson localization, *Physical Review B* **42**, 8121 (1990).
- [42] F. Evers and A. D. Mirlin, Anderson transitions, *Reviews of Modern Physics* **80**, 1355 (2008).
- [43] C. Groth, M. Wimmer, A. Akhmerov, J. Tworzydło, and C. Beenakker, Theory of the topological anderson insulator, *Physical review letters* **103**, 196805 (2009).
- [44] Y. Xing, L. Zhang, and J. Wang, Topological anderson insulator phenomena, *Physical Review B—Condensed Matter and Materials Physics* **84**, 035110 (2011).